Enabling simulations of helium bubble nucleation and growth: A strategy for interatomic potentials

X. W. Zhou,[1] N. C. Bartelt,[1] and R. B. Sills[1,2]
[1]*Sandia National Laboratories, Livermore, California 94550, USA*
[2]*Department of Materials Science and Engineering, Rutgers University, Piscataway, New Jersey 08854, USA*

(Received 19 March 2020; revised 7 October 2020; accepted 2 December 2020; published 13 January 2021)

Helium bubbles are a severe form of radiation damage that has been frequently observed. It would be possible to understand the complex processes that cause bubble formation if suitable interatomic potentials were available to enable molecular dynamics simulations. In this paper, Pd-H-He embedded-atom method potentials based on both Daw-Baskes and Finnis-Sinclair formalisms have been developed to enable modeling of He bubbles formed by the radioactive decay of tritium in Pd. Our potentials incorporate helium into an existing Pd-H potential while addressing two challenging paradoxes: (a) Interstitial He atoms can dramatically lower their energies by forming dimers and larger clusters in Pd but are only bound by weak van der Waals forces in the gas phase. (b) He atoms diffuse readily in Pd yet significantly distort the Pd lattice with large volume expansions. We demonstrate that both of our potentials reproduce density functional theory results for (b). However, the Daw-Baskes formalism fails to resolve paradox (a) because it cannot reproduce the experimental helium equation of state. We resolved this problem through a modification of the Finnis-Sinclair formalism in which a (fictitious) negative embedding charge density is produced by Pd at the He binding sites. In addition to molecular statics validation of static properties, molecular dynamics simulation tests establish that our Finnis-Sinclair potential leads to the nucleation of helium bubbles from an initial random distribution of helium interstitial atoms.

DOI: 10.1103/PhysRevB.103.014108

I. INTRODUCTION

Face-centered-cubic (fcc) palladium (Pd) has desirable properties for the storage of hydrogen isotopes [1,2] due to the reversibility of hydride formation at moderate temperatures and pressures. Its properties in the presence of tritium (T) are more stable than those of other metal tritides [3]. These properties also make palladium a valuable platform for study of the effects of helium (He) in metals. The decay of interstitial T to He leads to the formation of He bubbles due to the insolubility of He in Pd. As these helium bubbles grow [4], they cause swelling and change the T storage thermodynamics [5]. Eventually the Pd lattice is sufficiently disrupted that He is released rapidly [6]. Understanding He bubble nucleation and growth kinetics is thus important to the practical application of the tritides of palladium and other metals, as well as metals in other environments that introduce helium to the bulk, such as nuclear fission and fusion reactors [7,8]. While experimentally probing the complete evolution of T-induced bubbles requires times on the order of the half-life of T (12 years), molecular dynamics (MD) studies of He bubble nucleation and growth can be performed more quickly because the processes of nucleation and growth occur on atomistic simulation timescales, as will be demonstrated below. MD simulations, however, cannot be performed without a sufficiently accurate Pd-H-He interatomic potential. Note that T can be modeled as its isotope hydrogen (H) here because T and H have the same electronic structure. In the following, we will only refer to H.

For the binary Pd-H system, a potential should capture (i) the miscibility gap between dilute Pd and Pd hydride [9]; (ii) the preferred octahedral interstitial site for H [10]; (iii) the rapid H diffusion (activation energy barrier ~0.2 eV) [11]; as well as (iv) lattice constants, cohesive energies, and elastic constants of the PdH_x hydride as a function of composition x [12]. Numerous Pd-H potentials have been developed in the literature [13–18]. Some potentials [13,14] are designed only for dilute hydrogen compositions. These potentials either do not capture the miscibility gap or incorrectly predict a preference for tetrahedral hydrogen interstitial sites. The embedded-atom method (EAM) [13,19] potential developed by Wolf *et al.* [15,16] reported a miscibility gap, but unfortunately is not sufficiently well documented [17] to be regenerated. The EAM potential [17] we developed previously satisfies the four criteria outlined above, although the lattice constant of the H-rich PdH_x and the composition range of the miscibility gap deviate from experimental values [12].[1]

Given a Pd-H potential, a Pd-H-He potential can be constructed by defining the He-related component of the potential. For MD simulations of helium bubble nucleation and growth, the He component of the potential should capture a variety of properties as will be outlined here. Helium bubble formation is believed to occur in several stages. First, in defect-free Pd, interstitial He aggregates to form clusters, without creating new defects in the Pd lattice. When these clusters grow sufficiently large, Pd atoms are displaced to create a bubble. Thereafter the bubbles continue to grow by

[1]Recently, Park and Hijazi reported that their EAM Pd-H potential captures the miscibility gap with improved accuracy [18].

accumulating He and displacing Pd in a manner determined by the pressure of He in the bubbles. The He diffusion energy barrier is important for a potential to reproduce because it determines how fast He atoms form clusters. The bond length and bond energy of He-He dimers in Pd define how the He atoms cluster. The He cluster energy and vacancy formation energy of Pd as a function of cluster size determine when He bubbles nucleate from clusters. The swelling volume of interstitial He and (rocksaltlike) clusters determines the elastic effects of He on Pd and this in turn affects H storage thermodynamics. Finally, for capturing He densities within bubbles, a correct description of the equation of state of pure He is desired.

Two papers describing MD simulations of He behavior in palladium hydrides have been published recently [20,21]. The potential used in Ref. [20] incorrectly predicts tetrahedral interstitial sites for H. In addition, it is not clear if this potential can capture He bubble nucleation because He bubbles were manually created. We explored the potential used in Ref. [21] and found an extremely large He diffusion energy barrier in Pd (>3.0 eV). In contrast, the energy barrier found in the literature density functional theory (DFT) calculations is less than 0.48 eV [22]. In fact, our DFT calculations (to be presented below) indicate an even smaller He diffusion barrier (less than 0.1 eV). As a result, the literature potential used in Ref. [21] cannot realistically capture the kinetics of He bubble nucleation. Potentials have been created for He in W [23]. However, as we discuss below, the strategies used do not apply to He in octahedral sites in fcc Pd.

The objective of the present work is to extend our Pd-H EAM potential [17] to include He. This Pd-H potential is selected because it possesses a miscibility gap and its characteristics are well documented [11,12,17,24]. To capture all the DFT results on the He features elaborated above, we introduce an extension of the Finnis-Sinclair EAM formalism. We establish the usefulness of our approach by showing a MD study of the nucleation of He bubbles from randomly populated He interstitials, such as those produced experimentally by radiological decay of randomly distributed tritium atoms.

II. DENSITY FUNCTIONAL THEORY CALCULATIONS

The DFT calculations presented here are performed in a cubic 108 Pd atom cell. This unit cell size is chosen to diminish the possibility of artifacts due to shape distortions of the cells by the large effective size of interstitial He. We relax the positions of the atoms and calculated total energies using the VASP code [25,26], the Perdew-Burke-Ernzerhof (PBE) version of the generalized gradient approximation [27], and the projector-augmented wave approximation [28]. At least a $6 \times 6 \times 6$ set of k-vectors is used. We relax forces to be less than 0.001 eV/Å. In all calculations the shape and size of the unit cells are also relaxed to yield a stress-free state. Electronic relaxation is accelerated through Methfessel-Paxton Fermi level smearing [29] (width 0.2 eV). For accuracy, we use a 500-eV, plane-wave basis cutoff. To provide some estimate of the sensitivity to the choice of density functional, we also report some energies using the local density approximation (LDA).

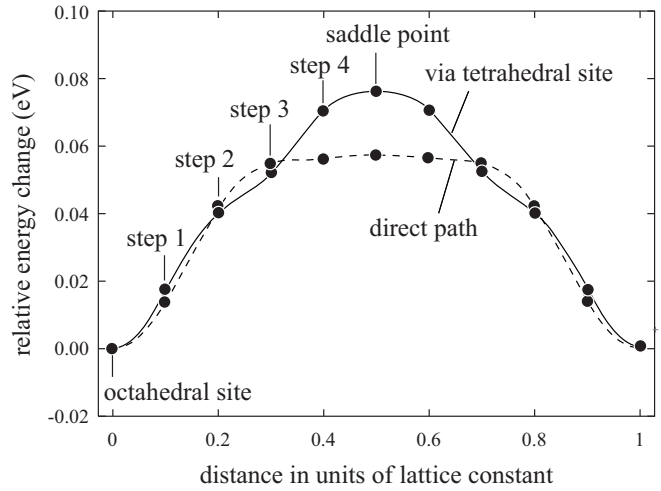

FIG. 1. He diffusion pathways between nearest neighbor octahedral sites in H-free Pd, as computed with DFT. Solid line: through tetrahedral site; dashed line: direct path.

First, consistent with the previous studies, we find that He preferentially occupies the octahedral interstitial site in Pd. The insertion energy is 3.64 eV, demonstrating the insolubility of He in Pd. Next, to estimate barriers for diffusion, the climbing-nudged elastic band method of Henkelman and colleagues [30–32] is used to compute diffusion pathways and transition states. There is some discrepancy in the literature in the location of the transition state for He diffusion between neighboring octahedral sites [33,34]. Zeng *et al.* [33] deduced a transition state at the intervening tetrahedral site, while Das and de Leeuw [22] and Cao and Geng [34] reported a transition state near the line connecting the neighboring octahedral sites. Based on our DFT computed diffusion paths given in Fig. 1, the direct path is preferred. For both paths, however, the diffusion energy barrier for an interstitial is only on the order of 0.1 eV, at the limits of what DFT can reasonably resolve. This small barrier is similar to what has been computed for He in W [35].

To gain insight into what determines the He diffusion barrier, we have computed how the electronic charge density rearranges during He motion. To do this we take the electronic charge density of the configurations along the direct path shown in Fig. 1 and subtract the sum of the charge densities of the identical Pd lattice without the He atom and the charge density of an isolated He atom. The resulting charge differences in the (100) plane containing the diffusion path are shown in Fig. 2. The solid circle marks the perimeter of a sphere containing 90% of the He electronic charge. As closed-shell atoms, He atoms clearly displace electrons toward the Pd [36]. The difference in the charge displaced from the indicated He sphere between the octahedral site and the transition state is only 0.08 e. However, even though the energy changes and differences in total charge displaced are relatively small, the nature of the charge displacement changes markedly during the He motion. The displacements at the transition state are of particularly long range, showing the necessity of considering large cells.

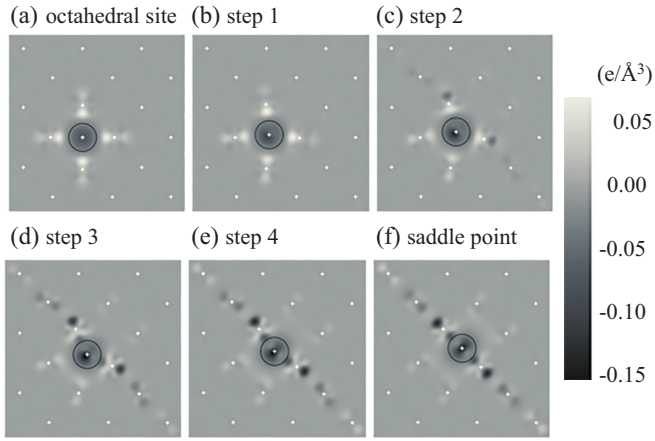

FIG. 2. (a)–(f) The electronic charge density displaced by a He atom along the diffusion path between the octahedral interstitial site and the direct transition state computed in Fig. 1. The white crosses mark atomic centers. The black circles contain 90% of the He electronic charge.

Figure 2 demonstrates that the two He electrons never chemically bind with the Pd lattice. Thus, the interstitial motion of He does not involve the forming, breaking, and reforming of chemical bonds, as is typical of interstitial atomic motion. The large charge rearrangements in Fig. 2 suggest, however, that Pd-Pd bonds are weakened and rearranged. This weakening presumably plays a role in our comparatively large DFT swelling volumes of 9.7 Å^3 of He in Pd.

Another unique aspect of interstitial He atoms is that, as reported below, they are strongly attractive within the Pd lattice with a binding energy of 0.9 eV. As argued below, this is due to the fact that clustering together reduces the overall charge displacement, rather than any chemical binding between He.

At low temperatures, it is well known that the equation of state of He is strongly affected by quantum mechanical, zero-point energy effects [37]. For example, ^{3}He at zero temperature can crystallize into the body-centered-cubic (bcc) structure, while ^{4}He crystallizes into the hcp structure. Thus the question naturally arises as to whether zero-point energy effects could influence the arrangement of He in Pd. To answer this question, we computed the zero-point energy of He containing lattices in the harmonic approximation. We calculated the normal vibrational modes ν_i of a cell containing two interstitial He atoms and 32 Pd atoms. We considered two configurations of the atoms, one in which the He atoms are initially placed in neighboring octahedral sites to form a He dimer and another one in which the He atoms are far from each other in fifth neighboring sites. We estimated the zero-point energy as $(1/2)\sum_i h\nu_i$. We find that the zero-point energy destabilizes the dimer by 40 (45) meV for ^{4}He (^{3}He). Thus, this effect is quite small compared to the overall effects of charge displacement, giving rise to an interaction energy of 0.9 eV, and justifies the neglect of He isotope effects in our empirical potential.

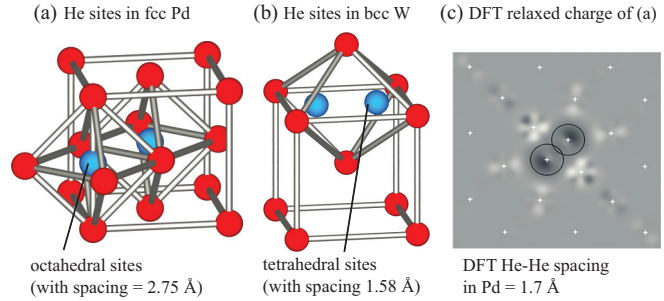

FIG. 3. The configuration of two neighboring He interstitial atoms in (a) fcc Pd and (b) bcc W. (c) shows the electronic charge displaced by a pair of He atoms in configuration (a) after structural relaxation using DFT. The gray scale in (c) is the same as in Fig. 2. Note that in contrast to Pd, two neighboring He atoms sit in one octahedral cage in W.

III. POTENTIAL FORMALISM

Two versions of Pd-H-He EAM potential are developed: one based on the Daw-Baskes (DB) formalism [13], and the other one based on the Finnis-Sinclair (FS) formalism [19]. Both formalisms consider two contributions to the potential energy: a pairwise interaction and a many-body interaction which is a function of the local electron density. However, the physical meaning of the many-body term is different between the two approaches. In DB, the many-body term accounts for the energetic cost of "embedding" an atom in the local electron cloud. In FS, the many-body term is derived from the second-moment approximation to the tight-binding framework. Rather than focusing on the differences in the physical interpretation of these terms, however, here we focus on—and leverage—their mathematical differences.

Mathematically, the electron density computation in the DB and FS formalisms differs in a subtle way. Considering that an atom j produces an electron density at a nearby location occupied by an atom i, the DB formalism assumes that this electron density depends only on the species of atom j, whereas the FS formalism assumes that this electron density depends on the species of both atoms i and j. Obviously, this difference in the DB and FS formalisms becomes inconsequential for elemental systems, but can critically influence the form of the potential for alloys and compounds (as we show here). As we now discuss, an extension of the FS formalism is necessary for us to resolve the paradoxical behavior that in a Pd matrix He atoms tend to form clusters, but in a pure He state He atoms only weakly interact through van der Waals forces.

In Figs. 3(a) and 3(b), we compare two neighboring helium interstitial sites in fcc palladium and bcc tungsten (W) using DFT. He tends to cluster in Pd because the two He atoms can collaborate in displacing the requisite electronic charge. Figure 3(c) shows the electronic charge displaced by the dimer formed after relaxing the configuration shown in Fig. 3(a). The He-He distance is 1.7 Å which is much shorter than the ~2.8 Å distance between octahedral sites. The total charge displaced by the dimer is 0.2 e less than the sum of the charge displaced by He in two separated octahedral sites. Further, as shown in Fig. 1, the energy required to displace an isolated He

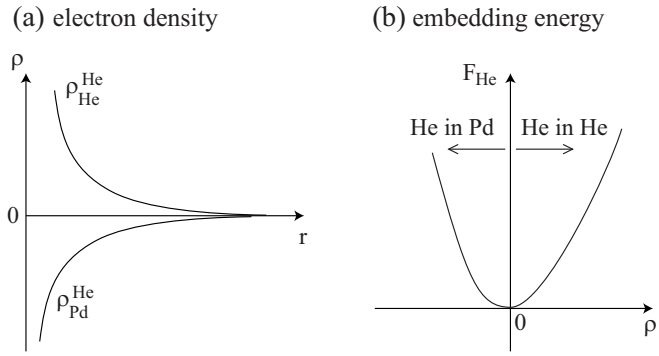

FIG. 4. Schematic depiction of FS functions. (a) Electron density ρ at a He atom is positive from He and negative from Pd. (b) Embedding energy as a function of electron density, showing how He-He interactions are attractive in Pd and repulsive in He. If a He atom in Pd is approached by another He atom, the embedding energy is reduced (attraction). In contrast, in pure He additional He interactions lead to embedding energy increases (repulsion).

atom along the same path that forms the dimer is small. The net result is that the He-He interaction energy has a strongly attractive value of ~ -0.9 eV.

The most straightforward way to reproduce this He dimerization in an EAM potential is to invoke an attractive He-He pairwise potential, as we do for the DB potential discussed below. However, this attraction introduces artifacts for the gas He phase in large bubbles since the attractive interaction between the He atoms is strictly a result of the 0.2 e reduction in the electron charge displacement within the Pd lattice. Another approach, which has been applied successfully for He in bcc W [23,38], is to introduce a repulsive Pd-He pairwise potential. However, as Fig. 3(a) shows, this repulsion will tend to center He in the octahedral sites making the He-He spacing even larger than the $\sim$2.8 Å spacing between the unexpanded octahedrons. Further, this repulsion directly affects lattice volume changes and He diffusion barriers. Because of these constraints, we were unable to find a Pd-He potential that was able to reproduce DFT results. As shown in Fig. 3(b) the situation for He dimers in W is much different because the preferred He binding position is in tetrahedral sites where neighboring distances are already small (although it is simpler to make He dimers low energy in W because of the tetrahedral site occupancy, the low energy structure of the He dimer in W computed in Ref. [35] is not neighboring tetrahedral sites).

We overcame this difficulty by extending the FS formalism to allow the designation of a negative Pd electron density $\rho^{He}_{Pd}(r)$ produced at He sites, without changing any EAM functions of the Pd-H system. While such a modification is not motivated by physics (since electron densities cannot be negative), it is consistent with the EAM formalism and enables us to capture the bifurcated behaviors of He in Pd compared with He in gas. A schematic depiction of the basic idea is presented in Fig. 4. Because He atoms prefer to occupy a site with zero electron density, we design a He embedding energy $F_{He}(\rho)$ that has a minimum at zero electron density. This means that a single He atom in Pd has a high embedding energy due to the negative electron density, correctly reproducing the insolubility of He interstitials in Pd lattices. Since by nature the He electron density $\rho^{He}_{He}(r)$ is positive at He sites, the magnitude of the negative electron density at a He atom in a Pd lattice is reduced when another He approaches. This reduces the embedding energy of both He atoms, effectively creating a strong attraction between them. On the other hand, in pure He environments the positive electron density $\rho^{He}_{He}(r)$ means that the magnitude of electron density, and therefore embedding energy, always increases when He atoms are closer. As a result, He-He interactions are purely repulsive in pure He using this potential.

Note that the FS potential derives from a second-moment approximation to the tight-binding framework [19,39,40]. Because the outer-shell electrons in He are saturated, the hopping integral between He and other atoms are zero [41]. This means that the many-body term in the original FS potential would define a zero bond order and hence a zero binding energy, leaving only the pairwise repulsive interaction energy. Our DFT calculations discussed above indicate that He is strongly repelled from regions with high electron density and a local electron density is generated by many atoms. As a result, the many-body effect of repulsion cannot be neglected (as the original FS formalism would imply for He). The mathematical form of the FS potential and the concept of negative electron density incorporate exactly the physics of this many-body repulsion, albeit through invoking a nonphysical electron density.

Since the FS formalism is more general than the DB formalism, we will use the FS formalism to represent both models in the following discussion for convenience. A complete Pd-H-He EAM model includes six pair interaction functions: $\phi_{PdPd}(r)$, $\phi_{PdH}(r)$, $\phi_{HH}(r)$, $\phi_{PdHe}(r)$, $\phi_{HHe}(r)$, $\phi_{HeHe}(r)$; nine electron density functions: $\rho^{Pd}_{Pd}(r)$, $\rho^{H}_{Pd}(r)$, $\rho^{He}_{Pd}(r)$, $\rho^{Pd}_{H}(r)$, $\rho^{H}_{H}(r)$, $\rho^{He}_{H}(r)$, $\rho^{Pd}_{He}(r)$, $\rho^{H}_{He}(r)$, $\rho^{He}_{He}(r)$; and three embedding energy functions: $F_{Pd}(\rho)$, $F_{H}(\rho)$, $F_{He}(\rho)$. The superscripts in the electron density functions signify which atoms occupy the location of the electron density measurement.

A. Daw-Baskes model

For the DB model, $\phi_{PdPd}(r)$, $\phi_{PdH}(r)$, $\phi_{HH}(r)$, $\rho^{Pd}_{Pd}(r) = \rho^{H}_{Pd}(r) = \rho^{He}_{Pd}(r)$, $\rho^{Pd}_{H}(r) = \rho^{H}_{H}(r) = \rho^{He}_{H}(r)$, and $F_{Pd}(\rho)$, $F_{H}(\rho)$ are taken directly from the corresponding functions of the literature Pd-H EAM [17]. Here we will develop three pair functions, $\phi_{PdHe}(r)$, $\phi_{HHe}(r)$, and $\phi_{HeHe}(r)$, one electron density function, $\rho^{Pd}_{He}(r) = \rho^{H}_{He}(r) = \rho^{He}_{He}(r)$, and one embedding energy function $F_{He}(\rho)$. The IJ pair function between He and Pd (i.e., IJ = PdHe) is assumed to be purely repulsive:

$$\phi_{IJ}(r) = E_{0,IJ}\exp\left(-\alpha_{IJ}\frac{r - r_{0,IJ}}{r_{0,IJ}}\right)f_c(r, r_{s,IJ}, r_{c,IJ}), \quad (1)$$

where $E_{0,IJ}$, α_{IJ}, $r_{0,IJ}$, $r_{s,IJ}$, $r_{c,IJ}$ are positive pairwise parameters, and $f_c(r, r_{s,IJ}, r_{c,IJ})$ is a cutoff function. $f_c(r, r_s, r_c)$ is defined as

$$f_c(r, r_s, r_c) = \begin{cases} \frac{1}{2}\mathrm{erfc}\left[\frac{\mu(r-r_s)+\nu(r_c-r)}{r_c-r_s}\right], & r < r_c \\ 0, & r \geqslant r_c \end{cases}. \quad (2)$$

Here μ and ν are constants defined by $\frac{1}{2}\mathrm{erfc}(\mu) = 10^{-5}$ and $\frac{1}{2}\mathrm{erfc}(\nu) = 0.9$, respectively. It can be shown that

$f_c(r, r_s, r_c)$ approaches 1 at $r \ll r_s$, and near 0 at r near r_c. As a result, multiplying $f_c(r, r_s, r_c)$ with any function will not change significantly that function at small r, but smoothly truncate the function at the cutoff distance r_c. Note that strictly speaking, $f_c(r, r_s, r_c) = 10^{-5}$ rather than 0 at $r = r_c$. However, we can set it to zero when constructing the tabular function for the MD code LAMMPS [42,43], which produces negligible errors.

In our DFT calculations, we observe that as He atoms closely approach H atoms and other He atoms in Pd, the energy of the system decreases. This indicates attractive He-H and He-He interactions in the Pd lattice. For the DB model, this attraction in fcc lattices can be effectively incorporated by the pair interaction. Hence, $IJ(IJ = \mathrm{HHe, HeHe})$ pair interactions involve an attractive component:

$$\phi_{IJ}(r) = \frac{E_{0,IJ} f_c(r, r_{s,IJ}, r_{c,IJ})}{\beta_{IJ} - \alpha_{IJ}} \left\{ \beta_{IJ} \exp\left[-\alpha_{IJ} \frac{(r - r_{0,IJ})}{r_{0,IJ}} \right] - \alpha_{IJ} \exp\left[-\beta_{IJ} \frac{(r - r_{0,IJ})}{r_{0,IJ}} \right] \right\}, \quad (3)$$

where $E_{0,IJ}$, α_{IJ}, β_{IJ}, $r_{0,IJ}$, $r_{s,IJ}$, $r_{c,IJ}$ are all pair parameters ($E_{0,IJ}$ is negative and all others are positive).

The electron density function for He is expressed as

$$\rho_I^J(r) = f_I^J \exp\left(-\gamma_I^J r\right) f_c\left(r, r_{s,I}^J, r_{c,I}^J\right), \quad (4)$$

where $I = \mathrm{He}$, $J = \mathrm{Pd, H, He}$, and f_I^J, γ_I^J, $r_{s,I}^J$, $r_{c,I}^J$ are positive pair parameters. Note $f_{\mathrm{He}}^{\mathrm{Pd}} = f_{\mathrm{He}}^{\mathrm{H}} = f_{\mathrm{He}}^{\mathrm{He}}$, $\gamma_{\mathrm{He}}^{\mathrm{Pd}} = \gamma_{\mathrm{He}}^{\mathrm{H}} = \gamma_{\mathrm{He}}^{\mathrm{He}}$, $r_{s,\mathrm{He}}^{\mathrm{Pd}} = r_{s,\mathrm{He}}^{\mathrm{H}} = r_{s,\mathrm{He}}^{\mathrm{He}}$, and $r_{c,\mathrm{He}}^{\mathrm{Pd}} = r_{c,\mathrm{He}}^{\mathrm{H}} = r_{c,\mathrm{He}}^{\mathrm{He}}$ in the DB model.

The He embedding energy function is assumed to have the form

$$F_{\mathrm{He}}(\rho) = \begin{cases} F_{0,\mathrm{He}}\left[\frac{1}{2} - \frac{1}{2}\cos\left(\frac{\rho}{\rho_{0,\mathrm{He}}}\pi\right)\right], & \rho < \rho_{0,\mathrm{He}} \\ F_{0,\mathrm{He}}, & \rho \geqslant \rho_{0,\mathrm{He}} \end{cases}, \quad (5)$$

where $F_{0,\mathrm{He}}$ and $\rho_{0,\mathrm{He}}$ are positive species-dependent parameters.

The functional forms described above are motivated by DFT calculations. Most importantly, our DFT calculations indicate that He atoms repel electrons toward the Pd sites. This means that electron densities at neighboring Pd sites are increased by He but the electron density at the He site is reduced. The increases in electron densities at Pd sites are captured by the positive He electron density function, Eq. (4). While the DB model does not allow the reduction of electron density at the He site, similar effects can be incorporated by reducing the sensitivity of He embedding energy to electron density. This is implemented in Eq. (5) where the embedding energy is a constant for the electron density range $\rho \geqslant \rho_{0,\mathrm{He}}$. This flat embedding energy also gives a low He diffusion energy barrier, resolving the paradox that He atoms have a low diffusion energy barrier while exhibiting a large swelling volume in Pd. As described above and will be shown below, the FS model better addresses the effects of electronic charge displacement through a positive He electron density at Pd and a negative Pd electron density at He.

B. Finnis-Sinclair model

In our FS model, the $\phi_{\mathrm{PdPd}}(r)$, $\phi_{\mathrm{PdH}}(r)$, $\phi_{\mathrm{HH}}(r)$, $\rho_{\mathrm{Pd}}^{\mathrm{Pd}}(r) = \rho_{\mathrm{Pd}}^{\mathrm{H}}(r)$, $\rho_{\mathrm{H}}^{\mathrm{Pd}}(r) = \rho_{\mathrm{H}}^{\mathrm{H}}(r)$, $F_{\mathrm{Pd}}(\rho)$, $F_{\mathrm{H}}(\rho)$ functions are taken directly from the corresponding functions of the literature Pd-H (DB) EAM potential [17]. Furthermore, we set $\rho_{\mathrm{H}}^{\mathrm{He}}(r) = -\rho_{\mathrm{H}}^{\mathrm{Pd}}(r)$ to ensure a negative electron density at He sites in PdH_x without additional tuning of the H electron density. The remaining functions to be determined include three pair functions: $\phi_{\mathrm{PdHe}}(r)$, $\phi_{\mathrm{HHe}}(r)$, and $\phi_{\mathrm{HeHe}}(r)$; four electron density functions: $\rho_{\mathrm{Pd}}^{\mathrm{He}}(r)$, $\rho_{\mathrm{He}}^{\mathrm{Pd}}(r)$, $\rho_{\mathrm{He}}^{\mathrm{H}}(r)$, $\rho_{\mathrm{He}}^{\mathrm{He}}(r)$; and one embedding energy function: $F_{\mathrm{He}}(\rho)$. With the FS model, the attractive H-He and He-He interactions in Pd can be obtained using the embedding energy so that purely repulsive pair interactions between He and any other element can be used. Here, we use Eq. (1) to represent $\phi_{\mathrm{PdHe}}(r)$ and $\phi_{\mathrm{HHe}}(r)$, and a repulsive polynomial to represent $\phi_{\mathrm{HeHe}}(r)$ (to more conveniently fit the He equation of state shown below) as in the following:

$$\phi_{\mathrm{HeHe}}(r) = \begin{cases} \alpha_{\mathrm{HeHe}}(r - r_{0,\mathrm{HeHe}})^2 + \beta_{\mathrm{HeHe}}(r - r_{0,\mathrm{HeHe}})^3, & r < r_{0,\mathrm{HeHe}} \\ 0, & r \geqslant r_{0,\mathrm{HeHe}} \end{cases}, \quad (6)$$

where α_{HeHe}, β_{HeHe}, and $r_{0,\mathrm{HeHe}}$ are positive pair parameters.

The electron density functions $\rho_{\mathrm{Pd}}^{\mathrm{He}}(r)$, $\rho_{\mathrm{He}}^{\mathrm{Pd}}(r)$, $\rho_{\mathrm{He}}^{\mathrm{H}}(r)$, and $\rho_{\mathrm{He}}^{\mathrm{He}}(r)$ are all represented by Eq. (4) except that $f_{\mathrm{Pd}}^{\mathrm{He}}$ is negative to enforce a negative Pd electron density at He sites.

The He embedding energy function $F_{\mathrm{He}}(\rho)$ is expressed as

$$F_{\mathrm{He}}(\rho) = \begin{cases} F_{0,\mathrm{He}}, & \rho \leqslant \rho_{0,\mathrm{He}} \\ F_{0,\mathrm{He}}\left[\frac{1}{2} - \frac{1}{2}\cos\left(\frac{\rho}{\rho_{0,\mathrm{He}}}\pi\right)\right], & \rho_{0,\mathrm{He}} < \rho < 0 \\ F_{2,\mathrm{He}}\rho^2 + F_{3,\mathrm{He}}\rho^3, & \rho \geqslant 0 \end{cases}, \quad (7)$$

where $F_{0,\mathrm{He}}$, $F_{2,\mathrm{He}}$, $F_{3,\mathrm{He}}$, and $\rho_{0,\mathrm{He}}$ are parameters ($\rho_{0,\mathrm{He}}$ is negative and $F_{0,\mathrm{He}}$, $F_{2,\mathrm{He}}$, and $F_{3,\mathrm{He}}$ are positive). Equation (7) has a minimum of zero at $\rho = 0$.

IV. POTENTIAL PARAMETRIZATION

Parametrization of the EAM potentials is accomplished by fitting DFT lattice constants and cohesive energies of six structures: Pd (fcc) with a He atom at an octahedral interstitial site, Pd with a He atom at a tetrahedral interstitial site, Pd with a He-He dimer at two neighboring octahedral interstitial sites, Pd with a H-He dimer at two neighboring octahedral interstitial sites, PdHe (rocksalt), and $PdH_{0.75}He_{0.25}$ (mixed rocksalt). In addition, we fit DFT lattice constants and cohesive energies for five additional structures corresponding to a He atom occupying different locations along the diffusion path in a Pd lattice. This helps fit the diffusion energy barrier. For the FS formalism, we also fit the energy of fcc He as a function of lattice constant. In reality, ^{3}He has a hexagonal close-packed crystal structure [44]. However, fitting fcc

TABLE I. Parameters for He-related EAM (DB) (length in Å and energy in eV).

$E_{0,\mathrm{PdHe}}$	0.002000	$r_{s,\mathrm{HHe}}$	4.295500	$\rho_{0,\mathrm{He}}$	13.742806	$f_{\mathrm{He}}^{\mathrm{He}}$	1.592508
α_{PdHe}	11.274271	$r_{c,\mathrm{HHe}}$	5.655147	$f_{\mathrm{He}}^{\mathrm{Pd}}$	1.592508	$\gamma_{\mathrm{He}}^{\mathrm{He}}$	0.221689
$r_{0,\mathrm{PdHe}}$	2.488746	$E_{0,\mathrm{HeHe}}$	−1.219337	$\gamma_{\mathrm{He}}^{\mathrm{Pd}}$	0.221689	$r_{s,\mathrm{He}}^{\mathrm{He}}$	2.575412
$r_{s,\mathrm{PdHe}}$	1.924805	α_{HeHe}	6.401310	$r_{s,\mathrm{He}}^{\mathrm{Pd}}$	2.575412	$r_{c,\mathrm{He}}^{\mathrm{He}}$	7.975412
$r_{c,\mathrm{PdHe}}$	2.319795	β_{HeHe}	2.680178	$r_{c,\mathrm{He}}^{\mathrm{Pd}}$	7.975412		
$E_{0,\mathrm{HHe}}$	−0.181660	$r_{0,\mathrm{HeHe}}$	1.680000	$f_{\mathrm{He}}^{\mathrm{H}}$	1.592508		
α_{HHe}	21.168969	$r_{s,\mathrm{HeHe}}$	3.289651	$\gamma_{\mathrm{He}}^{\mathrm{H}}$	0.221689		
β_{HHe}	12.057009	$r_{c,\mathrm{HeHe}}$	4.440681	$r_{s,\mathrm{He}}^{\mathrm{H}}$	2.575412		
$r_{0,\mathrm{HHe}}$	3.120972	$F_{0,\mathrm{He}}$	3.288065	$r_{c,\mathrm{He}}^{\mathrm{H}}$	7.975412		

is sufficient to tune the potential toward the experimental equation of state (a fluid equation of state is computed later during dynamic testing); obviously our potential will not accurately capture the ^{3}He solid phase, however. The fitting is achieved by minimizing the weighted mean-square difference between the target and predicted properties. Note that fitting static properties does not ensure good performance in MD simulations. An iterative approach is used to resolve this problem. Specifically, four built-in *Mathematica* [45] numerical optimization routines—a conjugate gradient method [46], the downhill simplex method of Nelder and Mead [47], a genetic algorithm [48], and a biased random walk (simulated annealing) [49]—are used for parametrization. After each fitting iteration, all four parametrized potentials are evaluated in MD simulations. These MD simulations include computation of the fluid equation of state for He and the energies of large He clusters in Pd, both of which are relevant to bubble nucleation and growth. The best performer during the test simulations is used as the starting potential for the next iteration, and target properties and weighing factors are adjusted based on the results of the MD evaluation. The iterations continue until one parametrized potential satisfactorily achieves the design criteria outlined above. The parameters thus determined are listed in Tables I and II, respectively, for the DB and FS formalisms. For convenience, the DB parameters are expressed in a more general FS form. Electronic versions of the potentials, in the format of the MD code LAMMPS [42,43], are provided in the Supplemental Material [50]. To show function shapes, plots of all the functions of the FS potential are also provided in the Supplemental Material. Note that existing LAMMPS pairstyle eam/fs does not allow negative electron densities and we have created a modified pairstyle eam/fs/he to enable them. This pairstyle will be included in a future LAMMPS release. The DB and FS potential files [50] use the eam/fs and eam/fs/he pairstyles, respectively.

V. CHARACTERISTICS OF POTENTIALS

A. Molecular statics calculations of basic properties

After a high-temperature MD test simulation validates that our potentials predict octahedral interstitial sites for He in Pd as found in our DFT calculations, detailed molecular statics (MS) simulations are performed to calculate important He-in-Pd properties that are relevant to bubble nucleation. These properties include the He diffusion energy barrier Q_{He}, the swelling volume $\Omega_{0,\mathrm{He}}$ of one He atom, the swelling volume $\Omega_{\mathrm{He,He}}$ of a second He atom nearest to the first He atom, the swelling volume $\Omega_{\mathrm{H,He}}$ of a He atom nearest to an existing H atom, energy E_{He} to insert a He atom in Pd, the bond length $r_{\mathrm{He\text{-}He}}$ and the bond energy $E_{\mathrm{He\text{-}He}}$ of two neighboring He atoms in Pd, the per He volume change $\Delta\Omega_{\mathrm{Pd}\rightarrow\mathrm{PdHe}}$(Å^3/He), and the energy change $\Delta E_{\mathrm{Pd}\rightarrow\mathrm{PdHe}}$ (eV/He) in making the rocksalt PdHe phase from fcc Pd and isolated He atoms. For all calculations with the fcc Pd lattice, we use $5\times5\times5$ unit cells. For all calculations with the rocksalt PdHe lattice, we use $6\times6\times6$ unit cells.

For validation of the potentials versus DFT, He diffusion is studied with the nudged elastic band methods [30–32]. We find that the lowest energy He diffusion path is between two neighboring octahedral interstitial sites, and hence we only calculate the energy barrier Q_{He} between octahedral sites. The swelling volume $\Omega_{0,\mathrm{He}}$ and insertion energy E_{He} for the first He atom are calculated as the corresponding differences in relaxed volumes and energies for systems with and without the He atom. The swelling volumes $\Omega_{\mathrm{He,He}}$ and $\Omega_{\mathrm{H,He}}$ for the

TABLE II. Parameters for He-related EAM (FS) (length in Å and energy in eV).

$E_{0,\mathrm{PdHe}}$	0.155004	$r_{c,\mathrm{HHe}}$	3.8101384	$\gamma_{\mathrm{He}}^{\mathrm{Pd}}$	0.8271817	$r_{s,\mathrm{He}}^{\mathrm{He}}$	1.5930120
α_{PdHe}	3.427897	α_{HeHe}	39.2759392	$r_{s,\mathrm{He}}^{\mathrm{Pd}}$	6.0267311	$r_{c,\mathrm{He}}^{\mathrm{He}}$	4.3285791
$r_{0,\mathrm{PdHe}}$	2.586950	β_{HeHe}	−4.0879424	$r_{c,\mathrm{He}}^{\mathrm{Pd}}$	7.0000000	$f_{\mathrm{Pd}}^{\mathrm{He}}$	−21.6766656
$r_{s,\mathrm{PdHe}}$	6.004509	$r_{0,\mathrm{HeHe}}$	1.7213068	$f_{\mathrm{He}}^{\mathrm{H}}$	4.6702433	$\gamma_{\mathrm{Pd}}^{\mathrm{He}}$	0.4897542
$r_{c,\mathrm{PdHe}}$	7.000000	$F_{0,\mathrm{He}}$	1.4084678	$\gamma_{\mathrm{He}}^{\mathrm{H}}$	0.8556600	$r_{s,\mathrm{Pd}}^{\mathrm{He}}$	3.1468368
$E_{0,\mathrm{HHe}}$	0.023764	$F_{2,\mathrm{He}}$	2.829678×10^{-6}	$r_{s,\mathrm{He}}^{\mathrm{H}}$	2.1333591	$r_{c,\mathrm{Pd}}^{\mathrm{He}}$	4.0352370
α_{HHe}	10.746122	$F_{3,\mathrm{He}}$	1.001682×10^{-8}	$r_{c,\mathrm{He}}^{\mathrm{H}}$	5.1412935		
$r_{0,\mathrm{HHe}}$	1.511214	$\rho_{0,\mathrm{He}}$	−39.9507951	$f_{\mathrm{He}}^{\mathrm{He}}$	101.9554550		
$r_{s,\mathrm{HHe}}$	2.559378	$f_{\mathrm{He}}^{\mathrm{Pd}}$	2.3805680	$\gamma_{\mathrm{He}}^{\mathrm{He}}$	0.4212486		

TABLE III. He-in-Pd properties calculated from MS (DB and FS potentials) and quantum mechanical (PBE and LDA) methods: He diffusion energy barrier Q_{He} (eV), He swelling volumes $\Omega_{0,\mathrm{He}}$, $\Omega_{\mathrm{He,He}}$, and $\Omega_{\mathrm{H,He}}$ (Å^3/He), He insertion energy E_{He} (eV/He), He-He bond length $r_{\mathrm{He\text{-}He}}$ (Å), and bond energy $E_{\mathrm{He\text{-}He}}$ (eV), per He volume change $\Delta\Omega_{\mathrm{Pd}\rightarrow\mathrm{PdHe}}$ (Å^3/He) and energy change $\Delta E_{\mathrm{Pd}\rightarrow\mathrm{PdHe}}$ (eV/He) for rocksalt PdHe formation.

Methods	Q_{He}	$\Omega_{0,\mathrm{He}}$	$\Omega_{\mathrm{He,He}}$	$\Omega_{\mathrm{H,He}}$	E_{He}	$r_{\mathrm{He\text{-}He}}$	$E_{\mathrm{He\text{-}He}}$	$\Delta\Omega_{\mathrm{Pd}\rightarrow\mathrm{PdHe}}$	$\Delta E_{\mathrm{Pd}\rightarrow\mathrm{PdHe}}$
DB potential	0.19	10.1	10.0	9.7	3.63	1.75	−0.87	9.2	2.92
FS potential	0.13	7.0	14.1	6.9	4.42	1.67	−2.00	10.5	3.35
PBE DFT	0.11	9.7	10.3	9.5	3.64	1.7	−0.87	6.7	2.99
LDA DFT	0.07	7.3	8.0	10.1	3.63	1.7	−0.85	7.4	2.96

second He atom are calculated as the corresponding difference in relaxed volumes for systems with and without the second He atom (placed at the nearest octahedral site to the first He or H interstitial). The bond length $r_{\mathrm{He\text{-}He}}$ is the relaxed atomic spacing between the two neighboring He atoms. The bond energy $E_{\mathrm{He\text{-}He}}$ is the energy change when two widely separated He interstitials become nearest neighbors at the octahedral sites. For instance, if the relaxed energies of systems containing no He atoms, one He atom, and two He atoms (at the neighboring octahedral sites) are, respectively, E_0, E_1, and E_2, then $E_{\mathrm{He\text{-}He}} = E_2 + E_0 – 2E_1$. The volume change $\Delta\Omega_{\mathrm{Pd}\rightarrow\mathrm{PdHe}}$ and energy change $\Delta E_{\mathrm{Pd}\rightarrow\mathrm{PdHe}}$ are derived from lattice constants and cohesive energies of fcc Pd and rocksalt PdHe. Calculated results of these properties are summarized in Table III along with our DFT results.

Table III indicates that, overall, both the DB and the FS potentials capture well the desired features of DFT values of all the listed properties. The He-He bond length obtained from both potentials is in good agreement with that from DFT. The diffusion energy barrier is slightly larger than DFT for both potentials, but still small enough to give large diffusivities. Both the DB and FS models slightly overestimate the volume change when a local rocksalt PdHe phase is formed. Furthermore, the FS model overpredicts the magnitude of the volume change and interaction energy of a He dimer as well as the insertion energy of a single He atom. Large magnitudes of these values are key to bubble nucleation but are difficult to capture by the conventional potentials. Despite the overprediction, however, the FS model will still accurately predict the nucleation of a bubble as will be shown below. Note that the He-He bond energy from DFT is around −0.86 eV and the FS bond energy is −2.00 eV. We point out that the magnitudes of these values are so large compared to k_BT that, once formed, a dimer will not disassociate, practically resulting in the same clustering behavior.

Based on our DFT calculations, the swelling volume of He is extremely large, $\Omega_{0,\mathrm{He}} \sim 10$ Å^3, from PBE and ~ 7 Å^3 from LDA (for reference, the H swelling volume is only ~ 2.7 Å^3). Our DB and FS potentials give $\Omega_{0,\mathrm{He}} \sim 10$ Å^3 and ~ 7 Å^3, respectively. Normally inserting a large atom into a small lattice would cause a large diffusion energy barrier because of the large lattice displacements required to move the inserted atom through a constricted transition state. Remarkably, our potentials can prescribe very low He diffusion energy barriers. It is our specific EAM functions that ensure both a large swelling volume and a low diffusion energy barrier.

B. Molecular dynamics calculations of helium equation of state

The He equation of state, typically described by the volume of a pure He phase (gas or liquid) as a function of pressure [51], is important for the He bubble growth processes. As a result, detailed MD simulations are performed to calculate atomic volume as a function of pressure for pure He based on both DB and FS potentials. For the DB potential, the system contains 12 × 12 × 12 fcc unit cells. For the FS potential, the system contains 10 × 10 × 10 fcc unit cells. Note that although we use an fcc initial structure, the system naturally becomes a liquid- or gaslike configuration with the FS model where He-He interactions are repulsive in the pure He phase. On the other hand, by using a classical potential we are neglecting the quantum mechanical effects which are important at low temperature (see, e.g., [52]).

Based on an *NPT* (constant number of atoms, pressure, and temperature) ensemble, the time-averaged atomic volume is calculated at a variety of pressures ranging from 1 to 22 kbar. Specifically, the systems are first annealed at 1000 K for 0.125 ns, and then at 300 K for another 1.0 ns. Time-averaged volumes are calculated for the last 0.5 ns. To accelerate simulations, we arbitrarily increase the He mass from 4 to 50 amu. This allows us to use a large time step $dt = 0.002$ ps without integration divergence [12,53]. Note that the increased mass only changes the kinetics but not the energetics that we are testing here. The results of the volume versus pressure relationship are shown in Fig. 5(a). For comparison, similar data from literature experiments [51] are included.

Figure 5(a) indicates that the DB model significantly underestimates the volume of pure He. This is because the DB potential invokes an attractive He-He interaction, which results in an unphysical condensed phase. In contrast, the results from the FS model capture well the experimental He equation of state. Note that experimental data may also have some uncertainty margin, and the differences between our model and experiments are competitive with other models [54]. A Lennard-Jones (LJ) pair potential was used for He in a previous study of He bubbles in Pd [21] and similar potentials have been used for He in W [23,38]. To compare the behavior of our FS potential with the LJ potential, we calculate cohesive energies of a model fcc He crystal as a function of the nearest He-He separation distance, and the results are shown in Fig. 5(b). Note that an fcc structure needs to be used as a medium to compare pair and EAM potentials. Figure 5(b) indicates that our He potential is very similar to the LJ potential except it is shifted to a larger interatomic distance by 0.1–0.2 Å and is designed to be purely repulsive.

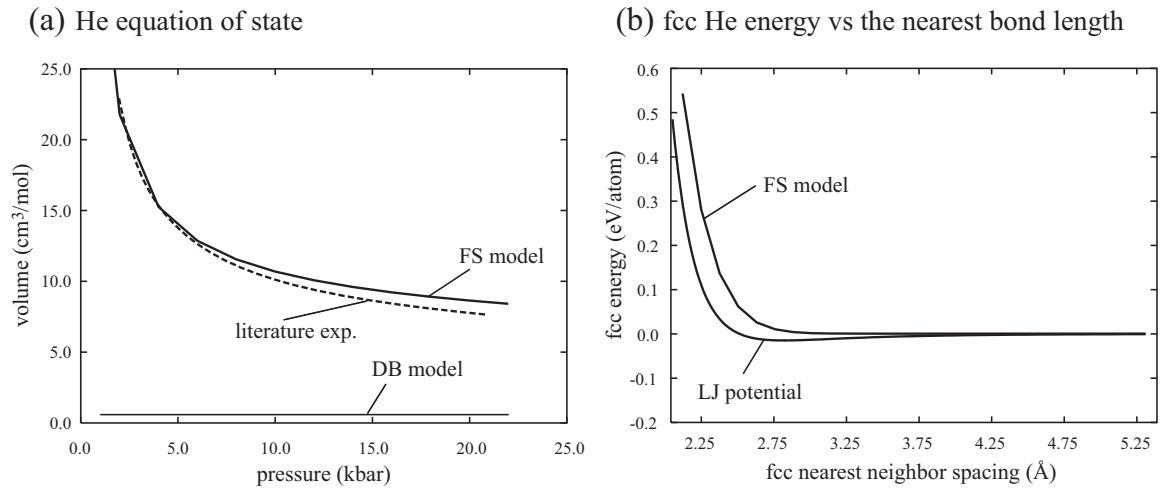

FIG. 5. (a) He equation of state at $T = 300$ K (experimental data from Ref. [51]) and (b) fcc He energy as a function of the nearest bond length compared to the LJ potential from Ref. [21].

This accounts for the slight overestimate of volumes in our computed equation of state. Figure 5 proves that the DB model is not ideally suited for studying late-stage He bubble growth because it cannot capture the He behavior of pure He in large bubbles despite the good fits to the He properties inside the Pd. As a result, we will focus on the FS model in the following.

C. Effects of He cluster size on He insertion energy and Pd vacancy formation energy

When He atoms are added into a Pd lattice, they segregate to form local He clusters in a rocksaltlike configuration because of the effective He-He attraction. As He cluster sizes increase, the system becomes unstable, eventually displacing a Pd atom from its lattice site to form a Pd vacancy-self interstitial (Frenkel) pair. A Pd vacancy with surrounding He atoms can be considered a He bubble nucleus. In principle, the He insertion energy as a function of He cluster size quantifies the stability prior to He bubble nucleation, while the Pd vacancy formation energy as a function of He cluster size measures the propensity of He bubble nucleation. The He insertion energy E_{He} listed in Table III is for a one-He cluster. We now further test the FS potential by using time-averaged MD simulations to calculate He insertion energy and Pd vacancy formation energy as a function of He cluster size.

Our MD systems include $20 \times 20 \times 20$ unit cells of fcc Pd. He atoms are sequentially added into the center of the cell, considering up to an eight-atom cluster. For each of these cases, two MD simulations are performed, one without a vacancy and one with a Pd vacancy near the center of the He cluster. Under a zero pressure *NPT* ensemble, MD simulations at $T = 300$ K are performed for 6.25 ns. After the first 1.25 ns is discarded, the final 5.00 ns simulations are used to derive time-averaged energies. These energies are used to calculate He insertion energies (per He atom) and Pd vacancy energies as a function of He cluster size (number of He atoms). The results of the calculated He insertion energies and Pd vacancy formation energies are shown, respectively, in Figs. 6(a) and 6(b). Similar calculations are performed using DFT methods, and the results are included in Fig. 6.

Table III indicates that the He insertion energy for a single He atom (i.e., E_{He}) is 4.42 eV for the FS potential and 3.64 eV for the DFT calculations. Both capture the large insertion energy that make an isolated He atom in the Pd lattice insoluble. Normalized with this E_{He}, Fig. 6(a) further indicates that the He insertion energy trends with respect to He cluster size agree between the FS and DFT calculations except when the He cluster contains seven atoms where the DFT value suddenly drops. We find that this is because when the cluster size reaches seven He atoms, in DFT a Pd atom is significantly displaced from its lattice site, resulting in the formation of a Pd interstitial-vacancy pair.[2] This interstitial does not form in MD simulations. We attribute the discrepancy to the significant difference in the system sizes between the MD and DFT calculations. We will explore the He cluster size needed to generate a Pd interstitial in MD simulations using a smaller system size below. Figure 6(a) also indicates that isolated He atoms tend to cluster because He insertion energy reduces with cluster size.

Figure 6(b) confirms that the Pd vacancy formation energy trends with respect to He cluster size are also similar between the FS and DFT calculations. Specifically, the Pd vacancy formation energy decreases with He cluster size, meaning that Pd vacancies (and hence bubbles) are more likely to form when the cluster size increases. Again, the DFT values jump abruptly at cluster size 7 due to the formation of a Pd interstitial. The absolute values of the Pd vacancy formation energies are higher for the FS than for the DFT calculations in Fig. 6(b). This means that bubbles are more likely to nucleate in DFT calculations (hence, the overestimation of the FS model on the He-He dimer swelling volume and He-He binding energy as shown in Table III does not cause premature formation of bubbles).

[2]In other words, the sum of the vacancy formation energy and self-interstitial energy has become negative. The DFT self-interstitial formation energy is 3.8 eV. A negative value for the sum for a seven-atom He cluster is consistent with the DFT trends shown in Fig. 5(b).

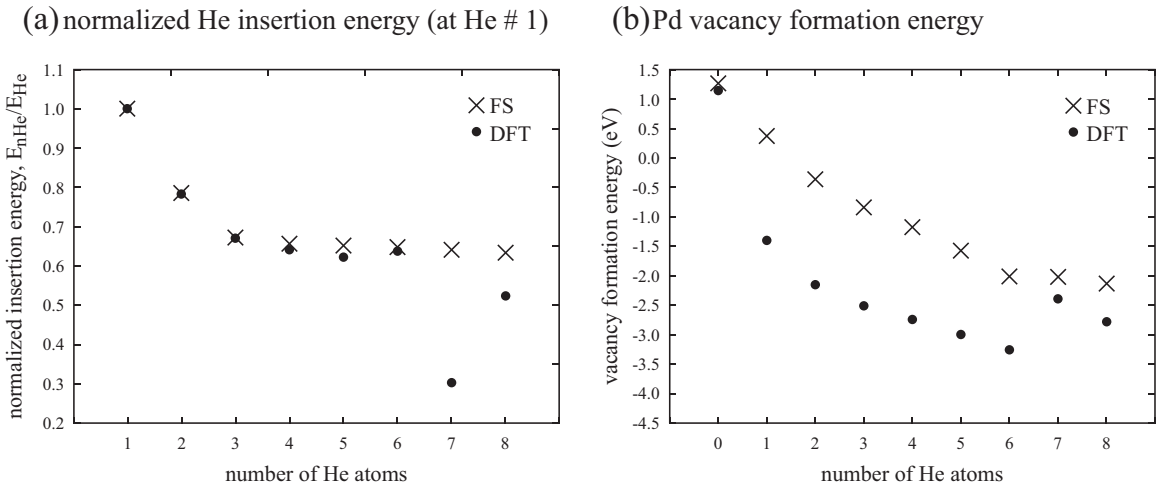

FIG. 6. Effects of He cluster size on (a) normalized He insertion energy and (b) Pd vacancy formation energy.

To explore if the system size difference contributes to the observed difference in self-interstitial formation shown in Fig. 6, we repeat the FS calculations using a system configuration shown in Fig. 7. Here the overall system dimension is the same as above, but the He clusters are periodically added into the system so that each periodic subcell is equivalent to the DFT cell size. The configurations obtained after MD simulations at $T = 10$ K for a period of $t = 5$ ns are shown in Figs. 7(a) and 7(b), respectively, for He cluster sizes of 6 and 7. In these figures, Pd interstitials are marked with small circles. It can be seen from Fig. 7(a) that after the MD annealing, none of the six-He clusters generate Pd interstitials. In sharp contrast, Fig. 7(b) shows that almost all of the seven-He clusters generate one or more Pd interstitials. These interstitials exhibit a dumbbell structure as shown in the inset, which matches the structure predicted by DFT. The formation of Pd interstitials at He cluster size 7 as predicted by the FS model is in excellent agreement with the DFT calculations. Given that our results using a large cell did not predict interstitial generation with a seven-He cluster, this result provides a warning about using small, highly distorted cells when studying He bubble nucleation processes.

VI. MOLECULAR DYNAMICS TESTS

MS simulations usually test limited scenarios. MD simulations often provide more stringent tests of empirical potentials. In previous MD simulations of He behavior in palladium hydrides, the He bubbles were manually created [20,21]. Now that our potentials capture a large swelling volume, a low diffusion energy barrier, a strong He-He attraction in Pd, and a He-He repulsion in He, MD simulations may directly reveal the nucleation of He bubbles. We now explore such MD capabilities using the FS potential (similar results were also obtained from the DB potential).

Our MD simulations employ $12 \times 12 \times 12$ unit cells of a $PdH_{0.6}He_{0.01}$ lattice modeling palladium tritide with a moderate interstitial concentration of He. As shown in Fig. 8(a), the initial configuration contains individual H and He atoms randomly populated in the octahedral interstitial sites of an fcc Pd lattice without bubbles. The system is then annealed

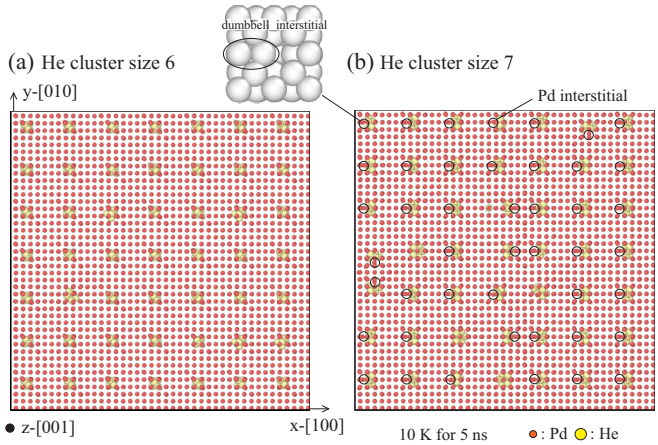

FIG. 7. Configurations obtained after 5-ns MD simulations at 10 K using the FS potential and small subcells: He cluster size of (a) 6 and (b) 7. Nucleated Pd self-interstitials are identified with circles.

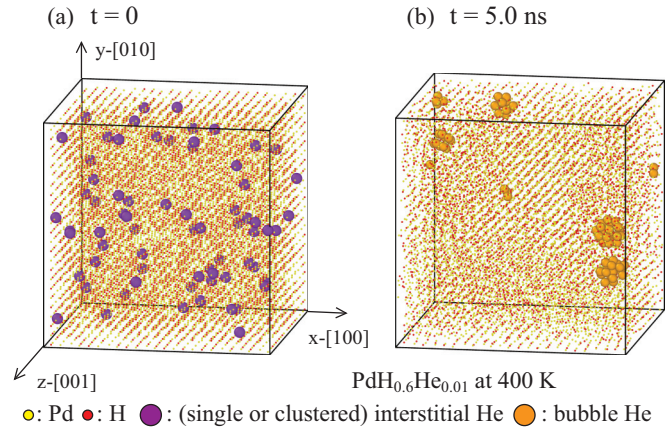

FIG. 8. MD annealing of a $PdH_{0.6}He_{0.01}$ structure at 400 K for 5.0 ns using the FS potential: (a) initial configuration and (b) final configuration.

at 400 K for 5 ns using a zero pressure *NPT* ensemble with a time step of $dt = 0.0005$ ps. The final configuration is shown in Fig. 8(b). Note that in Fig. 8, He atoms that have less than three Pd neighbors are colored orange; otherwise they are colored purple. Hence, purple atoms are single or clustered He interstitials, and orange He atoms are in bubbles.

Figure 8(b) indicates that the FS potentials predict the formation of He bubbles in palladium tritide at the end of the simulation. Thus, He atoms not only cluster, but also expel Pd atoms from lattice sites. Results shown in Fig. 8 indicate that our potentials can now enable MD simulations to directly reveal He bubble formation mechanisms in $PdH_{0.6}$ without any prior assumptions. Figure 8 also suggests that once multiple He atoms are present, nucleation of He bubbles from He interstitials is fast on MD timescales. Because bubbles are much more readily observed by experimental methods than interstitial atoms or vacancies, the ability to model bubble nucleation creates a path to model validation using experimental data (such as measurements made in the electron microscope).

VII. CONCLUSIONS

We have developed two Pd-H-He embedded-atom method potentials to enable molecular dynamics study of helium bubble nucleation and growth mechanisms. One potential is based on the Daw-Baskes formalism, and the other is an extension of the Finnis-Sinclair formalism. We demonstrate that both potentials can prescribe important properties relevant to the early stages of helium bubble formation, including the helium diffusion energy barrier, helium swelling volume, helium insertion energy, helium-helium bond length and bond energy, and swelling and formation energy of rocksalt PdHe clusters. We also demonstrate that our Finnis-Sinclair formalism further captures well the helium equation of state and the He cluster size effects on He insertion energy and Pd vacancy formation energy. Our direct molecular dynamics simulations reveal the nucleation of helium bubbles from randomly arranged helium interstitials. This unique capability opens opportunities for molecular dynamics studies of helium bubble nucleation without any prior assumptions on bubble configurations.

ACKNOWLEDGMENTS

Sandia National Laboratories is a multimission laboratory managed and operated by National Technology and Engineering Solutions of Sandia, LLC., a wholly owned subsidiary of Honeywell International, Inc., for the US Department of Energy's National Nuclear Security Administration under contract DE-NA-0003525.

The views expressed in the article do not necessarily represent the views of the US Department of Energy or the United States Government.

[1] T. B. Flanagan and W. A. Oates, The palladium-hydrogen system, Annu. Rev. Mater. Sci. **21**, 269 (1991).

[2] Y. Fukai, *The Metal Hydrogen System* (Springer, Berlin, Heidelberg, 1992).

[3] S. Thiebaut, M. Douilly, S. Contreras, B. Limacher, V. Paul-Boncour, B. Decamps, and A. Percheron-Guegan, ^{3}He retention in $LaNi_5$ and Pd tritides: Dependence on stoichiometry, ^{3}He distribution and aging effects, J. Alloys Compd. **446-447**, 660 (2007).

[4] S. Thiebaut, B. Decamps, J. M. Penisson, B. Limacher, and A. P. Guegan, TEM study of the aging of palladium-based alloys during tritium storage, J. Nucl. Mater. **277**, 217 (2000).

[5] L. B. Wang, M. Q. Lu, and Y. Y. Li, Tritium aging and its effect on the properties of metal tritides, Acta Metall. Sin. **39**, 449 (2003).

[6] D. F. Cowgill, Helium nano-bubble evolution in aging metal tritides, Fusion Sci. Technol. **48**, 539 (2005).

[7] *Fundamental Aspects of Inert Gases in Solids*, edited by S. E. Donnelly and J. H. Evans, NATO ASI Series B: Physics Vol. 279 (Plenum Press, New York, 1991).

[8] H. Trinkaus and B. N. Singh, Helium accumulation in metals during irradiation—where do we stand? J. Nucl. Mater. **323**, 229 (2003).

[9] R. T. Walters and M. W. Lee, Plateaus for palladium hydride and the effect of helium from tritium decay on the desorption plateau pressure for palladium tritide, Mater. Charact. **27**, 157 (1991).

[10] F. D. Manchester, A. San Martin, and J. M. Pitre, The H-Pd (hydrogen-palladium) system, J. Phase Equilib. **15**, 62 (1994).

[11] X. W. Zhou, T. W. Heo, B. C. Wood, V. Stavila, S. Kang, and M. D. Allendorf, Temperature- and concentration-dependent hydrogen diffusivity in palladium from statistically-averaged molecular dynamics simulations, Scr. Mater. **149**, 103 (2018).

[12] X. W. Zhou, T. W. Heo, B. C. Wood, V. Stavila, S. Kang, and M. D. Allendorf, Molecular dynamics studies of fundamental bulk properties of palladium hydrides for hydrogen storage, J. Appl. Phys. **123**, 225105 (2018).

[13] M. S. Daw and M. I. Baskes, Embedded-atom method: Derivation and application to impurities, surfaces, and other defects in metals, Phys. Rev. B **29**, 6443 (1984).

[14] M. S. Daw and M. I. Baskes, Semiempirical Quantum Mechanical Calculations of Hydrogen Embrittlement in Metals, Phys. Rev. Lett. **50**, 1285 (1983).

[15] R. J. Wolf, K. A. Mansour, M. W. Lee, and J. R. Ray, Temperature dependence of elastic constants of embedded-atom models of palladium, Phys. Rev. B **46**, 8027 (1992).

[16] R. J. Wolf, M. W. Lee, R. C. Davis, P. J. Fay, and J. R. Ray, Pressure-composition isotherms for palladium hydride, Phys. Rev. B **48**, 12415 (1993).

[17] X. W. Zhou, J. A. Zimmerman, B. M. Wong, and J. J. Hoyt, An embedded-atom method interatomic potential for Pd-H alloys, J. Mater. Res. **23**, 704 (2008).

[18] Y. H. Park and I. Hijazi, Development of physics based analytical interatomic potential for palladium-hydride, J. Mol. Model. **23**, 108 (2017).

[19] M. W. Finnis and J. E. Sinclair, A simple empirical *N*-body potential for transition-metals, Philos. Mag. A **50**, 45 (1984).

[20] C. N. Peng, The effects of hydrogen on the helium behavior in palladium, Nucl. Sci. Tech. **27**, 106 (2016).

[21] L. M. Hale, J. A. Zimmerman, and B. M. Wong, Large-scale simulations of helium-3 bubble growth in complex palladium alloys, J. Chem. Phys. **144**, 194705 (2016).

[22] N. K. Das and N. H. de Leeuw, Density functional theory study of the effect of helium clusters on tritium-containing palladium lattices, J. Phys.: Condens. Matter **27**, 475002 (2015).
[23] N. Juslin and B. D. Wirth, Interatomic potentials for simulation of He bubble formation in W, J. Nucl. Mater. **432**, 61 (2013).
[24] M. Ruda, E. A. Crespo, and S. R. de Debiaggi, Atomistic modeling of H absorption in Pd nanoparticles, J. Alloys Compd. **495**, 471 (2010).
[25] G. Kresse and J. Furthmuller, Efficiency of *ab-initio* total energy calculations for metals and semiconductors using a plane-wave basis set, Comput. Mater. Sci. **6**, 15 (1996).
[26] G. Kresse and J. Furthmuller, Efficient iterative schemes for *ab initio* total-energy calculations using a plane-wave basis set, Phys. Rev. B **54**, 11169 (1996).
[27] J. P. Perdew, K. Burke, and M. Ernzerhof, Generalized Gradient Approximation Made Simple. Phys. Rev. Lett. **77**, 3865 (1996).
[28] G. Kresse and D. Joubert, From ultrasoft pseudopotentials to the projector augmented-wave method, Phys. Rev. B **59**, 1758 (1999).
[29] M. Methfessel and A. T. Paxton, High-precision sampling for Brillouin-zone integration in metals, Phys. Rev. B **40**, 3616 (1989).
[30] G. Henkelman and H. Jonsson, Improved tangent estimate in the nudged elastic band method for finding minimum energy paths and saddle points, J. Chem. Phys. **113**, 9978 (2000).
[31] G. Henkelman, B. P. Uberuaga, and H. Jonsson, A climbing image nudged elastic band method for finding saddle points and minimum energy paths, J. Chem. Phys. **113**, 9901 (2000).
[32] A. Nakano, A space-time-ensemble parallel nudged elastic band algorithm for molecular kinetics simulation, Comput. Phys. Commun. **178**, 280 (2008).
[33] X. Zeng, H. Deng, and W. Hu, First-principles approach to the properties of point defects and small helium-vacancy clusters in palladium, Nucl. Instrum. Methods Phys. Res., Sect. B **267**, 3037 (2009).
[34] J. L. Cao and W. T. Geng, Migration of helium-pair in metals, J. Nucl. Mater. **478**, 13 (2016).
[35] C. S. Becquart and C. Domain, Migration Energy of He in W Revisited by *Ab Initio* Calculations, Phys. Rev. Lett. **97**, 196402 (2006).
[36] H.-B. Zhou, J.-L. Wang, W. Jiang, G.-H. Lu, J. A. Aguiar, and F. Liu, Electrophobic interaction induced impurity clustering in metals, Acta Mater. **119**, 1 (2016).
[37] J. Wilks, *The Properties of Liquid and Solid Helium* (Clarendon Press, Oxford, 1967).
[38] F. Sefta, K. D. Hammond, N. Juslin, and B. D. Wirth, Tungsten surface evolution by helium bubble nucleation, growth and rupture, Nucl. Fusion **53**, 073015 (2013).
[39] D. G. Pettifor, M. W. Finnis, D. Nguyen-Manh, D. A. Murdick, X. W. Zhou, and H. N. G. Wadley, Analytic bond-order potentials for multicomponent systems, Mater. Sci. Eng.: A **365**, 2 (2004).
[40] R. Drautz, D. A. Murdick, D. Nguyen-Manh, X. W. Zhou, H. N. G. Wadley, and D. G. Pettifor, Analytic bond-order potential for predicting structural trends across the *sp*-valent elements, Phys. Rev. B **72**, 144105 (2005).
[41] D. G. Pettifor, New Many-Body Potential for the Bond Order, Phys. Rev. Lett. **63**, 2480 (1989).
[42] LAMMPS download site: lammps.sandia.gov.
[43] S. Plimpton, Fast parallel algorithms for short-range molecular-dynamics, J. Comput. Phys. **117**, 1 (1995).
[44] S. G. Lipson, Helium crystals, Contemp. Phys. **28**, 117 (1987).
[45] S. Wolfram, *The Mathematica Book*, 5th ed. (Wolfram Research, Inc., Champaign, IL, 2004).
[46] M. R. Hestenes and E. Stiefel, Methods of conjugate gradients for solving linear systems, J. Res. Natl. Bur. Stand. **49**, 409 (1952).
[47] D. M. Olsson and L. S. Nelson, Nelder-Mead simplex procedure for function minimization, Technometrics **17**, 45 (1975).
[48] R. Storn and K. Price, Differential evolution—a simple and efficient heuristic for global optimization over continuous spaces, J. Global Opt. **11**, 341 (1997).
[49] S. Kirkpatrick, C. D. Gelatt, and M. P. Vecchi, Optimization by simulated annealing, Science **220**, 671 (1983).
[50] See Supplemental Material at http://link.aps.org/supplemental/10.1103/PhysRevB.103.014108 for the PdHHe potential table for the LAMMPS pairstyle eam/fs/he as well as plots of the fs potential functions.
[51] R. L. Mills, D. H. Liebenberg, and J. C. Bronson, Equation of state and melting properties of ^{4}He from measurements to 20 kbar, Phys. Rev. B **21**, 5137 (1980).
[52] U. K. Dieters and R. J. Sadus, *Ab initio* interatomic potentials and the classical molecular simulation prediction of the thermophysical properties of helium, J. Phys. Chem. B **124**, 2268 (2020).
[53] X. W. Zhou, F. El Gabaly, V. Stavila, and M. D. Allendorf, Molecular dynamics simulations of hydrogen diffusion in aluminum, J. Phys. Chem. C **120**, 7500 (2016).
[54] C. A. Walsh, J. Yuan, and L. M. Brown, A procedure for measuring the helium density and pressure in nanometre-sized bubbles in irradiated materials using electron-energy-loss spectroscopy, Philos. Mag. A **80**, 1507 (2000).